Controlled Pushing of Nanoparticles: Modeling and Experiments

Metin Sitti, *Member, IEEE,* and Hideki Hashimoto, *Member, IEEE*

***Abstract*—In this paper, a nano-robotic manipulation system using an atomic force microscope probe as the pushing manipulator and force and topology sensor is proposed. The task is the two-dimensional positioning of nanometer-size particles on a substrate in ambient conditions. Thus, the modeling of interaction forces and dynamics during the pushing operation is analyzed, and compared with the experimental results for an improved understanding of the nano scale physical phenomenon which is different from macro scale physics. Simulations and experiments are held for determining the conditions and strategies for reliable manipulation, and determining the affecting parameters. The results show that the latex particles with 242- and 484-nm radii can be positioned on Si substrates successfully with around 30-nm accuracy, and the behavior of the particle motion during pushing can be predicted from the experimental data.**

***Index Terms*—Atomic-force microscope, force control, micro/nano forces, micro/nano-mechatronics, nanoparticle assembly.**

I. Introduction

NANOTECHNOLOGY, which aims at the ideal miniaturization of devices and machines down to atomic and molecular sizes has been a recent hot topic as a promising high technology for the forthcoming century. By precise control of atoms, molecules, or nano scale objects, new sensors and man-made materials, tera-byte capacity memories, micro scale robots/machines, DNA computers, quantum devices, micro scale distributed intelligence system devices with integrated sensors, actuators and communication tools, etc., would be possible within the near future. However, for new nanotechnology products, there are still many challenges to be solved, and nano manipulation is one of the important challenges of the nano world. This kind of research is still immature since the physical and chemical phenomenon at this scale has not been completely understood, intelligent automatic precision manipulation strategies are not developed, and the specific tools for the specific applications have not been defined/designed clearly. Thus, the purpose of this paper is to propose an atomic-force-microscope (AFM)-based force-controlled pushing system with physical analysis of the manipulation tool (AFM tip) and nano scale object physical interaction for two-dimensional (2-D) positioning and assembly of nanoparticles.

Manuscript received December 15, 1999; revised February 1, 2000. Recommended by Guest Editors K.-M. Lee and B. Siciliano.

M. Sitti was with the Institute of Industrial Science, University of Tokyo, Tokyo 106-8558, Japan. He is now with the Robotics Laboratory, Department of Electrical Engineering and Computer Sciences, University of California, Berkeley, CA 94720 USA (e-mail: sitti@robotics.eecs.berkeley.edu).

H. Hashimoto is with the Institute of Industrial Science, University of Tokyo, Tokyo 106-8558, Japan.

Publisher Item Identifier S 1083-4435(00)05162-0.

The AFM is a three–dimensional (3-D) atomic resolution microscope which uses the interatomic force measurement principle for holding the topology images. Its mechanism is based on interatomic force interaction and, thus, can be applied to imaging of *all* types of particles/samples which are fully or semi-fixed on a substrate with homogenous surface stiffness and interatomic force properties. The AFM has also become popular as a simple manipulation tool [1]–[5]. Changing its function from only imaging to both imaging and manipulation, new challenging problems are introduced. At first, the particles on substrates should be *semi-fixed* in order to be able to move them. The solution to this problem could be using noncontact mode AFM imaging for not moving the particles during imaging as proposed in [2]. However, the selection of the absorption chemicals is a difficult issue depending on the type of the substrate and particle (for Au particles, Silane is used for Si subtrates [6], and Poly-L-Lysine for mica substrates [7]). Next, the mechanism of interatomic forces and dynamics should be understood for precise positioning of the particles [8]. However, the micro/nano mechanics for this kind of application have not been developed completely. Moreover, real-time monitoring of the manipulation process is almost impossible. Since the same tool is used as either the imaging or manipulation tool at a given instant, imaging is almost not possible during pushing operation. As one approach to this problem, researchers scan the area, where the target particle exists, before and after the manipulation [9], [1], [10], [11]. Thus, by using some fixed reference features, the new relative position of the particle is obtained from the images. However, this imaging is *offline*, and the unexpected problems during pushing cannot be detected. Another way is utilizing the force feedback information during pushing for reliable manipulation [12], [13]. A final approach would be using high-resolution external 2-D scanning electron microscope (SEM) imaging [14], although SEM can be utilized only in vacuum environments for some specific particles.

In this paper, possible solutions are proposed for the preceding challenging problems of AFM-based pushing manipulation. In our approach, pushing operation is modeled, real-time force feedback is utilized instead of real-time visual feedback or another external microscope during pushing, tapping-mode AFM imaging is used for offline visual feedback, and nanoparticles are pushed at the contact mode. A homemade open-structure AFM system with the piezoresistive deflection detection approach is constructed, and simulation and experimental results are compared for latex particle pushing applications. This paper is an extension of our work in [15], where the size of the particles are reduced by using AFM imaging instead of optical microscope (OM) imaging, particle

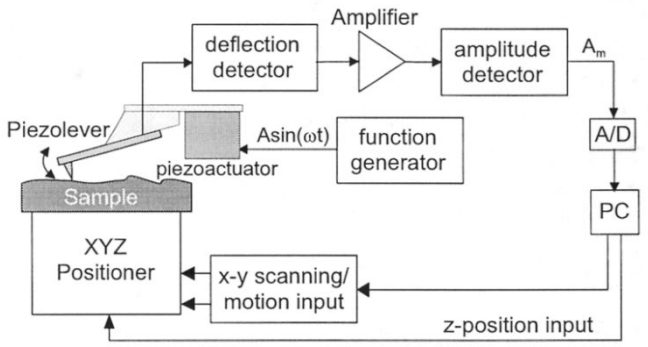

Fig. 1. Homemade noncontact imaging hardware.

motion behavior is predicted, new force-controlled pushing strategies are introduced, and dynamic analysis is improved.

The organization of the paper is as follows. In Section II, visual sensing at the nano scale is explained. Physical modeling of nano scale forces, sample preparation, and dynamics and control of the AFM cantilever are described in Sections III–V, respectively. Next, pushing mechanism and possible force-controlled pushing strategies are introduced in Section VI. Describing the system setup in Section VII, nanoparticle pushing simulation and experimental results are reported in Section VIII. Finally, conclusions with discussions and future directions are given in Section IX.

II. Visual Sensing: Tapping-Mode AFM Imaging

For the nano scale imaging, *tapping-mode* AFM imaging is utilized where the positions of the semi-fixed particles are minimally affected. In this mode, the cantilever (or sample) is oscillated using a piezoelectric stack actuator with known amplitude A and frequency f (close to the cantilever resonance frequency f_r) above the sample at the noncontact region. The homemade AFM system setup constructed for this kind of imaging is shown in Fig. 1. Mostly, $A = 10$–200 nm and $f = f_r \pm 100$ Hz. By moving the sample (or cantilever), the tip starts to tap the surface by switching between noncontact and contact regions. However, the contacts are instantaneous and, therefore, the applied normal load and lateral scanning forces are significantly reduced when compared to the contact imaging mode. During the tapping, measured A_m and f_m are changed due to the interatomic force gradient, and detecting these changes using lock-in-amplifier or frequency demodulation kind of electronic circuits, the change in amplitude ΔA, frequency Δf, or even phase $\Delta\phi$ can be measured. Observing a predefined change in these parameters, 3-D topology images can be held. An example of the change in the amplitude of the cantilever oscillation depending on the tip-sample distance $h(t)$ can be seen in Fig. 2. After starting to tap (point *A*), A_m is reduced by a slope until fully sticking to the surface at the point *B*. For imaging, a point on this slope such as *C* is selected for tracking this amplitude at each scanned x–y point on the surface (*C* should be as close as possible to *A* for reducing the load on the particles). In our setup, a typical AFM image scanning computation time is around 50 s for a 50×50 image size where it is limited by the x–y–z stage sampling rate.

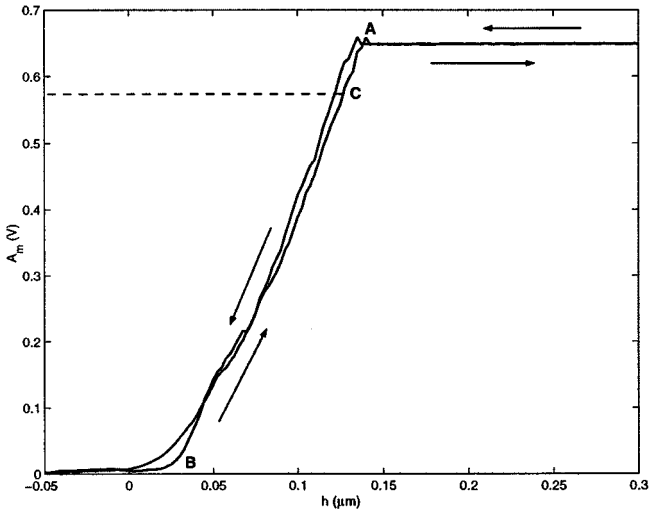

Fig. 2. A typical change in the cantilever vibration amplitude during tip-sample approach and retraction to a Silicon surface at the tapping mode imaging with $A = 100$ nm and $f = 133.4$ kHz ac excitation (experimental).

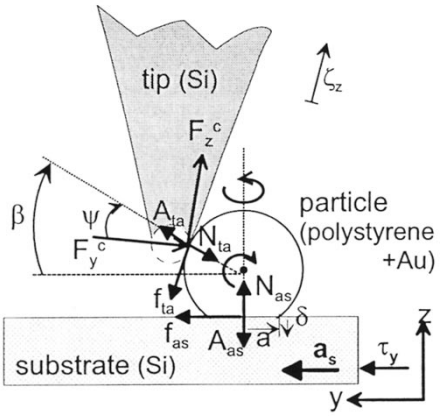

Fig. 3. Positioning of the nanoparticles by the AFM tip contact pushing, and the interacting forces.

III. Modeling of Interaction Forces in Air

Interaction forces among the AFM tip, particle (absorbate), and substrate before the tip contacts the particle, i.e., pushing, can be seen in Fig. 3. The AFM tip apex is assumed to be a spherical ball with radius $R_t = 10$–30 nm, and the particle radius is denoted as R_a. N_{as} and N_{as} are the repulsive contact forces, A_{as} and A_{ta} are the adhesion forces, and f_{as} and f_{ta} are the frictional forces for the particle substrate and tip particle, respectively. Elastic deformation of the particle is possible with contact radius of a, and indentation δ resulting from a resultant external load of P_z. Gravitational forces are relatively very small and, therefore, are neglected. These forces should be understood in order to control them for precise manipulation and interpret the cantilever force measurements [15]. The main components of the adhesion forces A_{as} and A_{ta} are van der Waals, capillary, and electrostatic forces. These forces, contact forces, and frictional forces are to be analyzed for modeling the interaction forces. As notation, the $(-)$ force means the attractive and $(+)$ means the repulsive forces.

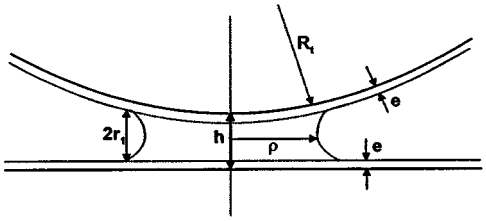

Fig. 4. Capillary force parameters during a sphere and flat surface contact.

A. Van der Waals Forces

Van der Waals forces exist for every material in every environmental condition (like the gravitational force in the macro world), and depends on the object geometry, material type and separation distance. Assuming the interaction of the spherical cantilever tip with a spherical absorbate/particle, the exact continuum mechanics solution becomes [16]

$$A_{ta}^{\mathrm{vdw}}(h) = -\frac{H(h+r_+)}{3}\left\{\frac{2R_aR_t}{h^2(h+2r_+)^2}+\frac{2R_aR_t}{((h+r_+)^2-r_-^2)^2} + \frac{1}{h(h+2r_+)}-\frac{1}{(h+r_+)^2-r_-^2}\right\} \quad (1)$$

where $r_+ = R_t + R_a$, $r_- = R_t - R_a$, R_t and R_a are the tip and particle radius, respectively, $h = h(t)$ is the tip–particle distance, and H is the Hamacker constant. In most cases, an $h \gg R_a$ kind of assumption is made for microparticles, but an exact solution would be more proper for the nanoparticles. Since there is always a liquid (water) layer on the sample in air conditions, $H = \{(H_{\mathrm{tip}} - H_{\mathrm{liquid}})(H_{\mathrm{particle}} - H_{\mathrm{liquid}})\}^{1/2}$ [17]. For the particle–substrate interaction, van der Waals force becomes

$$A_{as}^{\mathrm{vdw}}(h) = -\frac{H}{6}\left\{\frac{R_a}{h^2}+\frac{R_a}{(h+2R_a)^2}-\frac{1}{h}+\ln\frac{1}{(h+2R_a)}\right\}. \quad (2)$$

B. Capillary Forces

The water layer on the surfaces of the probe, particle, and substrate result in an adhesion force. A liquid bridge occurs between the tip and surface at close contact as shown in Fig. 4. The parameters of this capillary force are the tip–surface distance h, radii of curvature of the meniscus as r_1 and ρ, and the thickness of the liquid layer e. Using the macroscopic theory of the capillarity theory, the following model is held [18]:

$$A_{as}^{\mathrm{cap}}(h) = \left[\pi\rho^2\gamma_L\left(\frac{\cos\theta}{r_1}+\frac{1}{\rho}\right)+2\pi\gamma\rho\sin\theta+F_{SLS}^{as}\right] \cdot u(-h+L) \quad (3)$$

where

- θ contact angle;
- $u(.)$ step function;
- $L = L_l$ during approaching;
- $L = \delta$ during retraction.

$L_l \approx 2e$ is the thickness of the water layer, and δ is the breaking length of the meniscus which can be determined by the JKR contact mechanics modeling as $\delta = 0.132(12\pi R_a^{1/2}\gamma_L/K)^{2/3}$ where $1/K = [(1-\nu_a^2)/E_a + (1-\nu_s^2)/E_s]$, and E_a and E_s are the Young modulus, and ν_a and ν_s are the Poison's coefficients of the particle and substrate, respectively. r_1 can be approximated as $r_1 \approx -0.54/\log(P/P_s)$ nm using the Kelvin equation [17] assuming a water layer at 20 °C where P/P_s is the relative humidity ratio). γ_L is the liquid surface energy (for water $\gamma_L = 72$ mJ/m^2), and γ_{as}^{SLS} is the surface energy between solid–liquid–solid interface. Often, $\gamma_L > \gamma_{as}^{SLS}$, and the A_{as}^{SLS} force can be ignored. Finally, assuming $\theta \approx 0$ and $r_1 \ll \rho \ll R_a$, the A_{as}^{cap} reduces to

$$A_{as}^{\mathrm{cap}}(h) = 4\pi\gamma_L R_a\left(1-\frac{h-2e}{2r_1}\right)u(-h+L). \quad (4)$$

For the tip and particle, i.e., A_{ta}^{cap}, the above equations are changed such that $R_a \to \tilde{R}$ where $\tilde{R} = R_tR_a/(R_t+R_a)$, and $\gamma_L \to 2\gamma_L$.

C. Electrostatic Forces

Grounding a (semi)conducting substrate such as Si, Au, or HOPG, the electrostatic forces can be reduced. However, in the case of nonconducting particles, there are charges trapped around the perimeter of the particles, and during pushing or contact, triboelectrification introduces local charges. Since the particles are not picked up, the electrostatic force between the particle and substrate is not important. However, after pushing, the charge on the particle is transferred to the tip which can cause an electrostatic force between the particle and tip (then particles can stick to the tip during retraction which is observed in some cases experimentally). As a solution to this problem, the nonconducting polystyrene latex particles are coated with Au, and by grounding all the substrate and particles, electrostatic forces could become negligible. However, a model for the electrostatic forces is still desirable for general cases.

It is assumed that all objects are free of charge at the beginning. However, after contacting the objects, contact electrification and triboelectrification occur, and forces due to these charges should be computed.

For the work functions of ϕ_1 and ϕ_2 of two surfaces, the resulting voltage difference is $U = (\phi_1 - \phi_2)/e$ where $e = 1.6\times10^{-19}$C is the e^- charge. Then, the electrostatic force becomes

$$A_{ta}^{el}(h) = -\frac{\epsilon_0 U_{as}^2 S_{ta}}{2h^2} \quad (5)$$

where ϵ_0 is the permittivity, and S is the shared area. $S_{ta} = 4\pi\tilde{R}r_1$, and $U_{ta} = 0.25$ V for the Au-coated particle surface and Si tip. For the Au-coated particle and Si substrate, $S_{as} = 4\pi R_a r_1$, and $U_{as} = 0.5$ V. Then, for $R_t = 30$ nm, $R_a = 250$ nm, $r_1 = 1.7$ nm, and $h < 10$ nm, A_{ta}^{el} is in the order of 10 s of pN which can be almost neglected.

D. Repulsive Contact Forces

Since the contact area between the particle and tip is very small, only the deformation between the particle and substrate along the z axis is considered [19]. In the contact region, the repulsive elestic deformation/indentation forces with surface adhesion are to be modeled (plastic deformations are excluded in this study). Assuming small load and high surface forces, the JKR contact model [20] is selected for approximate contact area

prediction. Adding the short-ranged adhesion forces, for spherical tip and flat surface, the JKR model results in the following equations:

$$\begin{aligned} P_z &= Ka^3/R_a - \sqrt{3\pi\omega K a^3} \\ \delta &= a^2/R_a - 2/3\sqrt{3\pi\omega a/K} \\ a^3 &= R_a/K\left(P_z + 3\pi R_a\omega + \sqrt{6\pi R_a\omega P_z + (3\pi R_a\omega)^2}\right) \end{aligned} \tag{6}$$

where ω is the adhesion energy.

E. Frictional Forces

During pushing, the friction between the particle and substrate plays an important role. The definition of the friction at the micro/nano scale can be given as

$$f_{as} = \mu_{as} N_{as} \tag{7}$$

where $N_{as} = A_{as} + F_{as}^{l}$ with $A_{as} = 4\pi R_a \gamma_L$ at contact and F_{as}^{l} is the external load, and μ_{as} is the particle–substrate friction coefficient. Also, there is a friction between the tip and particle such that $f_{ta} = \mu_{ta} N_{ta}$ with $N_{ta} = A_{ta} + F_{ta}^{l}$, and $A_{ta} = 2\pi\tilde{R}\gamma_L$.

IV. Sample Preparation

Preparation of dispersed nanoparticles is a challenging issue, and JEOL Company particles which are dispersed with a scattering gun on a Si substrate are utilized for the experiments. As the design issue, the above forces should be checked for the selected particle and substrate geometry and material type, and environmental conditions such that:

- during tip–particle approach and separation, the adhesion forces should not result in sticking of the particles to the tip;
- maximum static frictional force should be smaller than the applied load in order to be able to move a particle.

More detailed analysis results in the following conditions for holding the above features:

$$R_a > 0.5\tilde{R}\sin\beta \tag{8}$$

$$\mu_{as}^{s} \geq \frac{\tilde{R}\cos\beta}{2R_a} = \frac{\cos\beta}{2(1 + R_a/R_t)} \tag{9}$$

where μ_{as}^{s} is the maximum static friction coefficient for the particle–substrate interaction. The first equality is correct for all R_t and R_a for $\beta \in [0, \pi/2)$. For the second one, μ_{as}^{s} is calculated depending on R_a where $R_t = 30$ nm is fixed in our system. For $R_a = 10$ nm, $\mu_{as}^{s} \geq 0.014$, and for $R_a = 1000$ nm, $\mu_{as}^{s} \geq 0.35$. Here, μ_{as}^{s} cannot be selected arbitrarily since, then, the particle may not be pushed. For reducing this problem, μ_{as}^{s} should be selected as $\mu_{as}^{s} \approx \cos\beta/2(1 + R_a/R_t)$, and a stiff cantilever should be used for enough pushing load.

V. Cantilever Dynamics and Position Control

Denoting the deflections along the x, y, and z axes as ζ_x, ζ_y, and ζ_z, respectively, as shown in Fig. 5, the deflection vector is defined as $\boldsymbol{\zeta} = [\zeta_x \ \ \zeta_y \ \ \zeta_z]^T$. Taking the force vector as $\boldsymbol{F^c} = [F_x^c \ F_y^c \ F_z^c]^T$, and assuming the cantilever with the z-axis

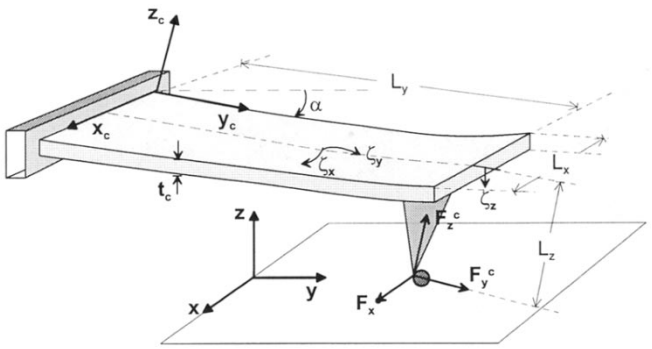

Fig. 5. AFM cantilever bending along x–y–z axes during pushing nano objects.

stiffness of k_c is tilted by an angle of α along the x axis for preventing the collision between the piezolever and substrate, the deflection is determined by the forces as follows [21]:

$$\begin{aligned} \boldsymbol{\zeta} &= \boldsymbol{C}\boldsymbol{F^c} \\ \boldsymbol{C} &= \frac{1}{k_c}\begin{bmatrix} c_1 & 0 & 0 \\ 0 & c_2 & c_3 \\ 0 & c_3 & 1 \end{bmatrix} \end{aligned} \tag{10}$$

where $c_1 = 2L_z^2/L_y^2 + t_c^2/L_x^2$, $c_2 = 3L_z^2/L_y^2$, $c_3 = 3L_z/(2L_y)$, L_x, L_y, and L_z are the cantilever lengths along the x–y–z axes, and t_c is the cantilever thickness. Thus, the important point is that the cantilever cannot be modeled as three decoupled springs for an accurate modeling where y and z axes are coupled. Using our piezoresistive deflection measurement system, only ζ_z can be measured (also, ζ_x can be measured by the optical detection method or a new piezolever design which is our future work). Then, the measured deflection corresponds to

$$\zeta_z = (c_3 F_y^c + F_z^c)/k_c. \tag{11}$$

Thus, F_y^c lateral force also has an effect on ζ_z, and can be directly observable from ζ_z.

Piezoelectric x–y–z actuators are utilized for atomic resolution positioning. These actuators have hysteresis and drift problems depending on the motion duration and range, and temperature changes. For imaging, since x–y motion consists of scanning with specified constant range, actuators can be calibrated offline using laser interferometry, and these calibration data then can be used for accurate scanning (in the case of commercial AFM's). However, in manipulation tasks, the tip moves on arbitrary user-defined or automatically defined points in a given range; thus, open-loop control is not reliable. Therefore, the best method is to integrate high-resolution sensors such as capacitive, strain gauge, linear variable differential transformer (LVDT), or optical sensors to motion axes for closed-loop control. In our system, a Physick Instrumente x–y–z closed-loop stage (P-762.3L) with 10-nm resolution, 0.1% hysteresis error, and 100-μm range in all axes is utilized for the initial experiments, and a new stage with <1 nm accuracy using capacitive sensors and a digital signal processor (DSP) control is under installation. The dynamics of the stage along the y axis can be given as [22]

$$\frac{1}{\omega_y^2}\ddot{y}_s + \frac{1}{\omega_y Q_y}\dot{y}_s + y_s = \tau_y - f_{as} \tag{12}$$

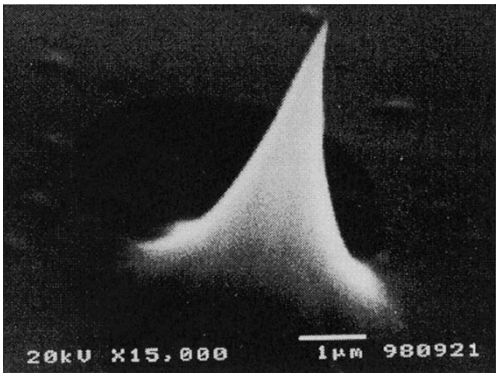

Fig. 6. SEM photo of the silicon piezoresistive cantilever tip with apex radius of 20–30 nm (PSI Company).

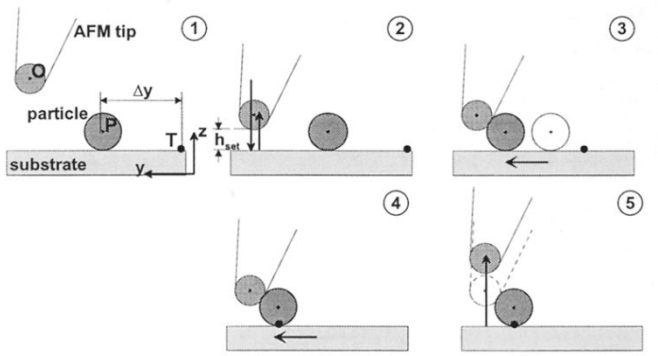

Fig. 7. AFM-based automatic 1-D particle pushing strategy. $1 \rightarrow 2$: automatic parking; $2 \rightarrow 3$: tip–particle contact detection; $3 \rightarrow 4$: pushing; and $4 \rightarrow 5$: tip retraction.

where $\omega_y = 2\pi f_y$, $f_y = \sqrt{k_y/m_s}/(2\pi) = 250$ Hz is the y-stage resonant frequency with m_s and k_y the stage and sample total mass and k_y the y-axis stage stiffness, $Q_y = 20$ is the amplification factor, y_s denotes the sample y-axis position, and τ_y is the stage driving force.

VI. Manipulation Strategy

In this study, Au-coated latex particles absorbed on Si substrates are to be pushed using an Si fabricated AFM cantilever tip (Fig. 6) in ambient conditions. At first, the images of particles are obtained using AFM tapping-mode imaging, as explained in Section II. Then, for a one–dimensional (1-D) pushing example, AFM-based pushing is realized by the motion steps as shown in Fig. 7.

- $1 \rightarrow 2$ (*auto-parking*): The tip is automatically moved at the z direction until detecting the contact by the substrate by measuring the cantilever deflection (absolute tip–substate distance is not known initially), and retracted back to a predetermined parking height h_{set}.
- $2 \rightarrow 3$ (*automatic tip–particle contact detection*): The tip is moved along the substrate until detecting the particle by cantilever deflection detection, and then stopped.
- $3 \rightarrow 4$: The particle is pushed for a desired distance Δy by moving the substrate (or the tip) with a constant speed,
- $4 \rightarrow 5$: After completing the pushing operation, retracting back to the initial height occurs.

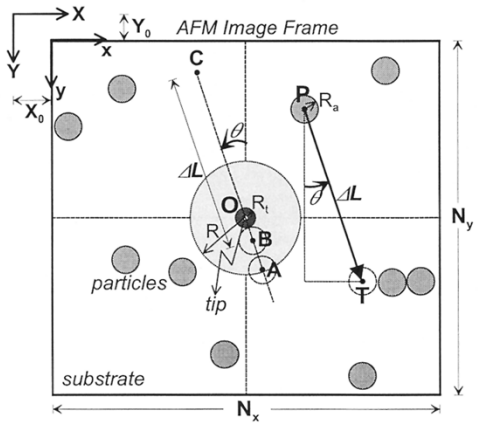

Fig. 8. Coordinate frames of the 2-D AFM image graphics display during the semi-autonomous particle pushing.

For a 2-D pushing manipulation, an additional step before *2* is required for initial aligning of the particle through the pushing direction.

A. Semi-Autonomous Pushing Scheme

After AFM imaging, the tip is located above and to the center of the image coordinates with a preset value of $z_{\text{park}} = z_c + h_{\text{set}}$ where z_c is the final tip-substrate contact z position. The resulting AFM image frame coordinates and components in the 2-D graphics user interface can be seen in Fig. 8. (x, y) denotes the AFM image coordinate frame with micrometer units, and (X, Y) stands for the stage x–y micrometer position coordinates. The relation between both coordinates can be given as

$$(X, Y) = (x + X_0, y + Y_0) \tag{13}$$

where (X_0, Y_0) are the initial positions during the AFM imaging. The points *O*, *P*, and *T* in the figure represent the AFM tip center, manually selected particle center, and user-defined target position, respectively. The aim of the automatic control scheme is "*to push the particle at P to the point T precisely.*" Assuming the stage x–y positioning is precise (closed-loop control), and the substrate is moved instead of the AFM tip where the tip behaves as a stopper during pushing, the proposed pushing scheme for enabling this control is as follows.

1) Initially, $(x_O, y_O) = (N_x/2, N_y/2)$ where N_x and N_y are the AFM image x and y micrometer sizes, and (x_P, y_P) and (x_T, y_T) points are known. Thus, the distance ΔL, the pushing direction θ, and the initial approach point *A* coordinates are computed as

$$\begin{aligned}(\Delta x, \Delta y) &= (x_T - x_P, y_T - y_P)\\ \Delta L &= \sqrt{\Delta x^2 + \Delta y^2}\\ \theta &= \arctan(|\Delta y|/|\Delta x|)\\ (s_x, s_y) &= (|\Delta x|/\Delta x, |\Delta y|/\Delta y)\\ (x_A, y_A) &= (x_O + s_x R \sin\theta, y_O + s_y R \cos\theta)\end{aligned} \tag{14}$$

where $R = 3R_a + R_t$.

2) Initial positioning before pushing: move stage from *P* to *A* by setting $(X, Y) = (X_0 + x_A - x_P, Y_0 + y_A - y_P)$.

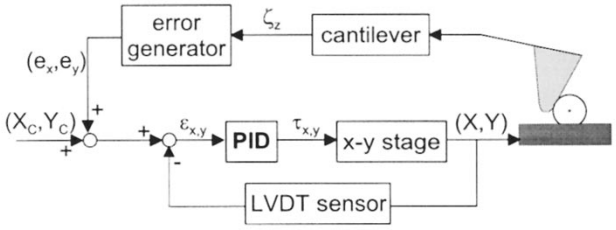

Fig. 9. Constant height control pushing strategy.

3) Contact point *B* detection: move from **A** through **O** until $F_z^c = k_c\zeta_z < T_z$ with $T_z > 0$ is the predefined contact force threshold.
4) Contact pushing through the point *C*, i.e., $(x_C, y_C) = (x_B - s_x\Delta L\cos\theta, y_B - s_y\Delta L\sin\theta)$.
5) Returning to the initial positions: move stage to (X_0, Y_0) and automatically park to the z_{park} height.

B. Pushing Control Strategies

For stopping the particle at *B* precisely and, thus, moving the particle from *B* to *C*, two different control strategies are proposed: *constant height control* and *constant contact force control.* Since there is no real-time visual feedback of the particle position, only the real-time ζ_z feedback can be utilized during the pushing control. The control parameter is the stage x–y–z position.

1) Pushing Controller I—Constant Height Control: Assuming that the substrate surface is parallel to the x–y motion plane, i.e., $\beta \neq \beta(X, Y)$, the x–y stage is moved to the target position (X_C, Y_C) using proportional–integral–derivative (PID) control while the stage z position is kept constant in this pushing control approach, as shown in Fig. 9. The tip–particle contact force F_z^c is observed at each (X_i, Y_i), $i = 1, \cdots, \Delta L/\Delta$ where Δ is the x–y motion step size. From the F_z^c and $\dot{F}_z^c$ data, x–y positioning errors can be predicted as (e_x, e_y) for a precise positioning. The error generator computes the following error sources.

1) *Static Friction Sticking at the Beginning*: The particle sticks to the substrate during the initial pushing due to the static friction, and an x–y offset value of (x^*, y^*) which should be compensated. These offset values are computed directly from the experimental data as the stage x–y motion from the tip–particle contact point C_1 (first $F_z^c > 0$ point) to the shearing point C_2 which is the first F_z^c peak after C_1, or $\dot{F}_z^c = 0$ point, as shown in Fig. 10.
2) *Tip–Particle Contact Loss*: During pushing, the tip–particle contact can be lost due to the x–y positioning errors at *B*, and the rotation/spinning of the particle along the z axis during pushing. Therefore, the contact loss point C_3 should be detected automatically for stopping the pushing operation after this point. C_3 is detected from the F_z^c data as the next $F_z^c = 0$ point after C_2 where F_z^c keeps on as zero (during rolling motion $F_z^c = 0$ is possible with periodic intervals, and these points are eliminated by checking the few following points whether they also stay at zero or not). After detecting C_3 at the (X_3, Y_3) position, the x–y motion is stopped by setting the error values as $(e_x, e_y) = (X_3 - X_C, Y_3 - Y_C)$.

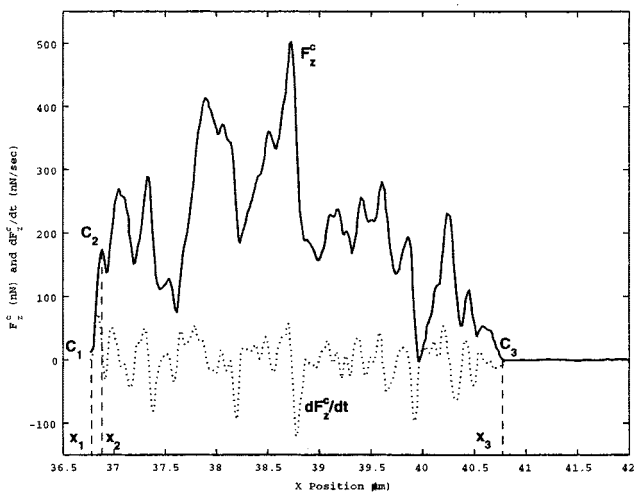

Fig. 10. An example of the F_z^c and $\dot{F}_z^c$ data during constant height pushing for the case of losing contact after C_3 point.

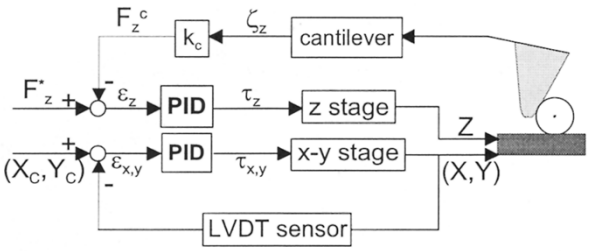

Fig. 11. Control scheme for the constant contact force-based pushing strategy.

If the pushing operation is stopped by the contact loss, then the stage is moved to the point *A* back, the particle is assumed not to change its position, or searched by tapping-mode AFM imaging; after detecting the new particle center position in the new image, it is set to *A* if its center is shifted, and the pushing scheme steps *3* and *4* are repeated until there is no contact loss stop.

2) Pushing Controller II—Constant Contact Force Control: In this controller, the contact force instead of the z position is kept constant by F_z^c feedback, and PID z positioning control, as shown in Fig. 11. The reference F_z^* value is determined by preliminary pushing test experiments. As the advantage of this controller with respect to the first one, the pushing operation is not affected by the substrate surface topology changes, or the substrate surface and x–y motion surface alignment errors. However, the only problem arises if the tip slips from the particle surface, and contacts with the substrate instead of the particle during pushing. This case could be rare for a sliding type of particle motion, but it becomes possible if the particle rolls. Slow pushing and careful design of the tip–particle friction/sticking can eliminate this problem.

C. Pushing Mechanism

For understanding the particle motion behavior during the pushing manipulation depending on the proposed control strate-

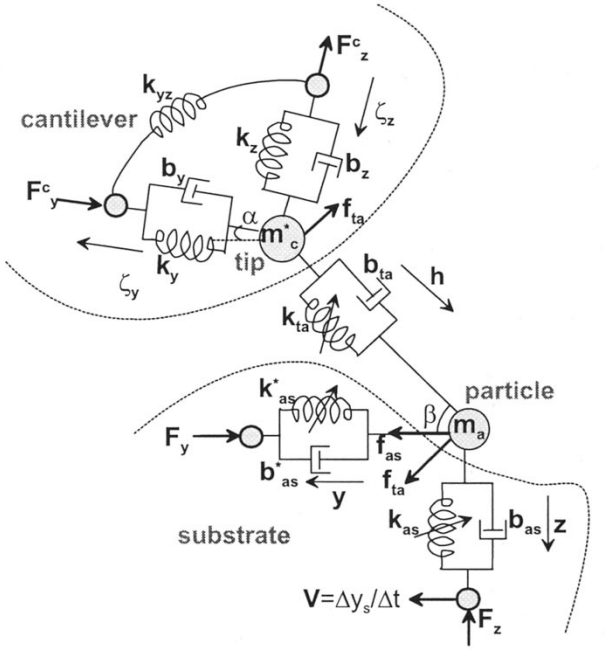

Fig. 12. Point-mass model of the contact pushing mechanism along the y axis.

gies, a theoretical modeling could help to understand and interpret the experimental results. For simplifying the notations and graphs, the particle is assumed to be pushed along the y axis where the same notation and models can be extended to the x–y motion case directly. Assuming the AFM cantilever is reduced to a point mass at the apex of the tip, the point mass model of the interaction forces during pushing are shown in Fig. 12. The parameters in the model are given as follows: $k_z = k_c$, $k_y = k_c/c_2$, $k_{yz} = k_c/c_3$, and $b_z = b_y = 2\pi f_r m_c^*/Q_c$ where f_r is the cantilever resonant frequency and Q_c is the quality factor in air, $m_c^* = k_z/(4\pi^2 f_r)$ is the cantilever effective mass, m_a is the particle mass, $V = \Delta y_s/\Delta t$ is the *constant* y-stage speed, h is the tip–particle indentation depth, $F_{as} = N_{as} - A_{as}$, $F_{ta} = N_{ta} - A_{ta}$, $k_{as}^* = 8R_aG^*$ with $G^* = ((2-\nu_a)/G_a + (2-\nu_s)/G_s)^{-1}$ where G_a and G_s are the shear modulus for the particle and substrate, respectively, z is the particle–substrate indentation depth, $k_{ta} = -\partial F_{ta}/\partial h$, b_{ta} is the tip–particle damping term which is negligible, $k_{as} = -\partial F_{as}/\partial z$, b_{as} is the particle–substrate damping, $k_{as}^* = 0.85k_{as}$ [23], and $b_{as}^* \approx 0$.

During the pushing operation, there are two main phases: static friction and kinetic friction regions. At the beginning, due to the static friction, the particle and tip follow the stage motion along the y axis to the point where the applied cantilever load exceeds the static friction between the particle and substrate. In this region, the following equations are held at the equilibrium points assuming a slow motion:

$$\begin{aligned} f_{as} &= F_y^c \cos\alpha + F_z^c \sin\alpha \\ F_{as} &= F_y^c \sin\alpha - F_z^c \cos\alpha \\ F_y^c &= k_y y \cos\alpha \\ F_z^c &= k_z y \sin\alpha \\ \zeta_y &= F_y/k_y + F_z/k_{yz} \\ \zeta_z &= F_z/k_z + F_y/k_{yz} \\ F_y &= k_{as}^* y. \end{aligned} \tag{15}$$

Here, $y = y_s$ and $z = \delta$ from the JKR model using (6) with $P_z = F_{as}$. At the shearing point $y = y^*$ and $f_{as} = \mu_{as}^s(F_{as} + A_{as})$. Then, y^* can be computed as

$$y^* = \frac{\mu_{as}^s 4\pi R_a \gamma_L}{k_y \cos^2\alpha + k_z \sin^2\alpha - \mu_{as}^s \sin\alpha\cos\alpha(k_y - k_z)}. \tag{16}$$

From this relation, the condition for enabling the particle pushing can be given as $y^* \geq 0$, which means that $\mu_{as}^s \leq (k_y \cot\alpha + k_z \tan\alpha)/(k_y - k_z)$. For example, for $\alpha = 15°$, $k_z = 8$ N/m and $k_y = 1427$ N/m, $\mu_{as}^s \leq 3.45$. Connecting this equality with (9)

$$\frac{\cos\beta}{2(1+R_a/R_t)} \leq \mu_{as}^s \leq \frac{k_y \cot\alpha + k_z \tan\alpha}{k_y - k_z}. \tag{17}$$

After the particle is separated from the substrate surface, the main dynamics of the particle or tip due to the constant V speed can be obtained as follows:

$$\begin{aligned} m_c^*\ddot{\zeta}_y + b_y\dot{\zeta}_y + k_y\zeta_y &= F_y^c + F_z^c k_y/k_{yz} \\ m_c^*\ddot{\zeta}_z + b_z\dot{\zeta}_z + k_z\zeta_z &= F_z^c + F_y^c k_z/k_{yz} \\ I_0\ddot{\theta} &= (f_{as} - f_{ta})R_a + f_\theta \\ m_a\ddot{y} + b_{as}^*\dot{y} + k_{as}^* y &= f_{as} + f_{ta}\sin\beta - F_{ta}\cos\beta \\ m_a\ddot{z} + b_{as}\dot{z} + k_{as} z &= F_{as} - F_{ta}\sin\beta - f_{ta}\cos\beta \\ f_{as} &= F_{ta}\cos\beta - f_{ta}\sin\beta \\ F_{as} &= F_{ta}\sin\beta + f_{ta}\cos\beta \\ F_y^c &= k_y y\cos\alpha - F_{ta}\cos\gamma + f_{ta}\sin\gamma \\ F_z^c &= k_z y\sin\alpha - F_{ta}\sin\gamma - f_{ta}\cos\gamma \end{aligned} \tag{18}$$

where $I_0 = 2m_aR_a^2/5$ is the moment of inertia of the particle, f_θ is the rolling resistance between the particle and surface [15], and $\gamma = \beta - \alpha\,\mathrm{sgn}(\beta - \alpha)$. After separation, the following motion behavior cases may occur: pure sliding, stick–slip motion, rotation, or rolling. Assuming that the particle is purely sliding ($f_{as} = \mu_{as}^k F_{as}$ where μ_{as}^k is the kinetic friction coefficient), the tip is not sticking to the particle ($f_{ta} = \mu_{ta}^k F_{ta}$), and $h \approx 0$, the following equalities can be held at the steady state:

$$\begin{aligned} \zeta_y &= y\cos\alpha - (F_y^c/k_y + F_z^c/k_{yz}) \\ \zeta_z &= y\sin\alpha - (F_z^c/k_z + F_y^c/k_{yz}) \\ |f_\theta| &> |(f_{as} - f_{ta})R_a| \\ F_{ta} &= \mu_{as}^k(\mu_{ta}^k\cos\beta A_{ta} + A_{as})/ \\ &\quad (\cos\beta/(1+\sin\beta) - \mu_{as}^k(\mu_{ta}^k\cos\beta + \sin\beta)) \\ f_{ta} &= F_{ta}\cos\beta/(1+\sin\beta) \\ y &= \zeta_y\cos\alpha + \zeta_z\sin\alpha + \Delta y_s \\ \Delta y &= (\zeta_y\sin\alpha - \zeta_z\cos\alpha)\sin\beta\cos\beta \\ \Delta z &= (\zeta_y\sin\alpha - \zeta_z\cos\alpha)\sin^2\beta \\ \beta &\to \arctan\{(R_a\sin\beta + \Delta z)/(R_a\cos\beta - \Delta y)\} \\ F_z &= k_y\zeta_y\sin\alpha - k_z\zeta_z\cos\alpha \\ z &= \delta(F_z). \end{aligned} \tag{19}$$

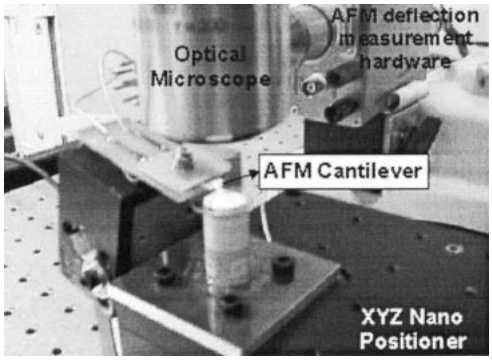

Fig. 13. Homemade open-structure AFM system photo.

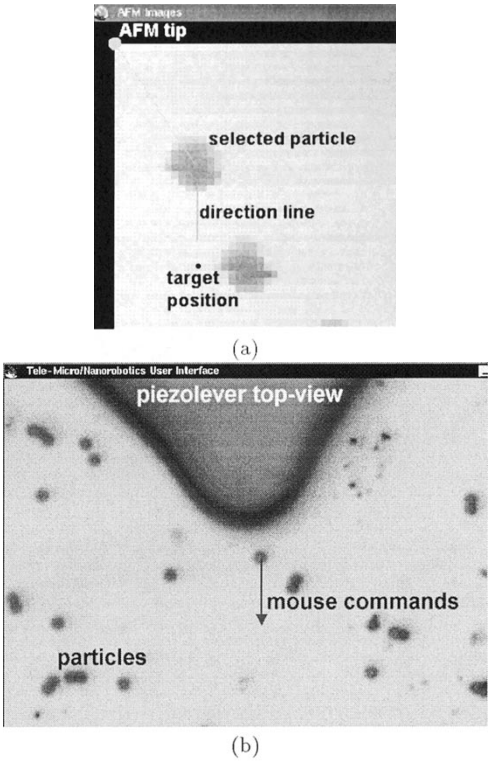

Fig. 14. Graphical user interface during task-based pushing control. (a) AFM gray-scale image window for nano scale imaging and motion commands. (b) Micro scale high-resolution optical microscope real-time image window.

VII. System Setup

For conducting experiments, a homemade open-structure AFM system (Fig. 13) with task-based graphical user interface is utilized [24]. Piezoresistive cantilevers where the silicon cantilever has a doped boron layer which changes its resistance due to the deflection moment are utilized [25]. This type of cantilever could be the future micro scale robot grippers as the integrated sensor probes. The graphical user interface consists of a real-time rough top-view OM image window and offline AFM greyscale image window, as seen in Fig. 14. In both windows, cantilever tip position, selected particle to be pushed, and the user-defined target positions are displayed. The selected particle is pushed automatically through the target point by the proposed pushing strategies.

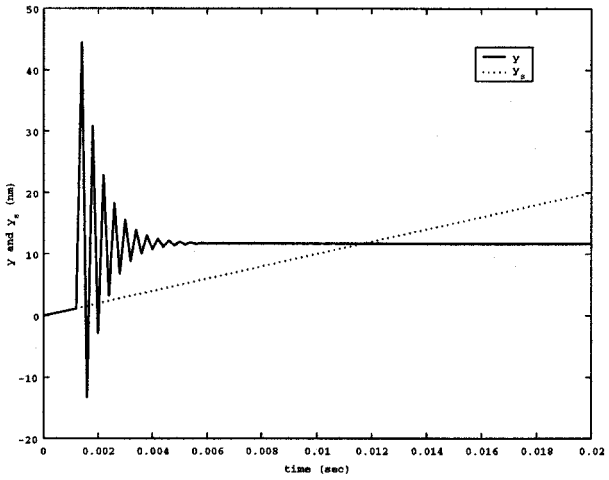

Fig. 15. The settling of the y position of the particle as a function of the stage y position y_s during pushing for the sliding particle motion case.

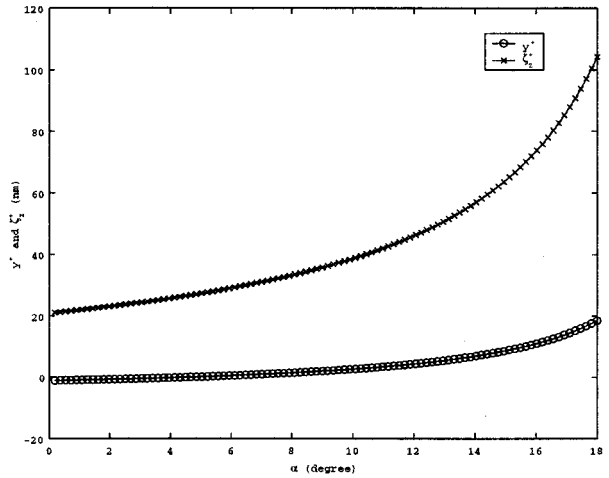

Fig. 16. The effect of changing α on y^+ and ζ_z^+.

VIII. Experiments and Simulations

Using the proposed models, the effect of different parameters such as β, α, μ_{as}^s, and R_a are observed by simulations. During the simulations, if that parameter is not the changing one, the parameter values are selected as follows: $k_z = 8$ N/m, $\mu_{as}^s = \mu_{ta}^s = 0.3$, $\mu_{as}^k = \mu_{ta}^k = 0.2$, $R_a = 242$ nm, $R_t = 30$ nm, $V = 1$ μm/s, $L_y = 155$ μm, $L_z = 6.7$ μm, $\alpha = 15°$, $\beta = 30°$, $\gamma_L = 72$ mJ/m^2, $\nu_s = 0.27$, $\nu_t = 0.3$, $E_s = 169$ GPa, and $E_t = 70$ GPa. Assuming only the pure-sliding case and the contact point between the tip and particle is at $y = 0$, the y position of the tip is given in Fig. 15 for the case of pure sliding where y settles to a constant y^+ at the steady state (also ζ_z settles to ζ_z^+). At first, the effect of the cantilever tilt angle α on y^+ and ζ_z^+ is observed. From Fig. 16, it can be seen that, within a limited range of α, ζ_z^+ and y^+ increase with the increasing angle. Secondly, changing the tip–particle contact angle β (β settles to the values given in Fig. 17 during sliding), it can be deduced from the Fig. 18 that the optimum selection of β can result in a minimum $y^+ = y^*$ error at the beginning of the

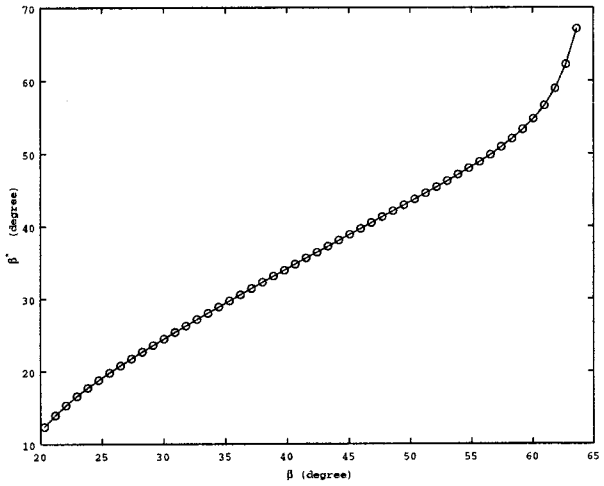

Fig. 17. The converged β values (β^*) for different initial β values.

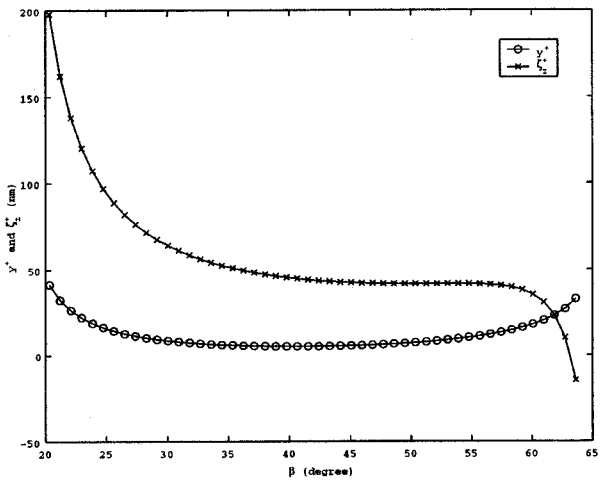

Fig. 18. The effect of changing β on y^+ and ζ_z^+.

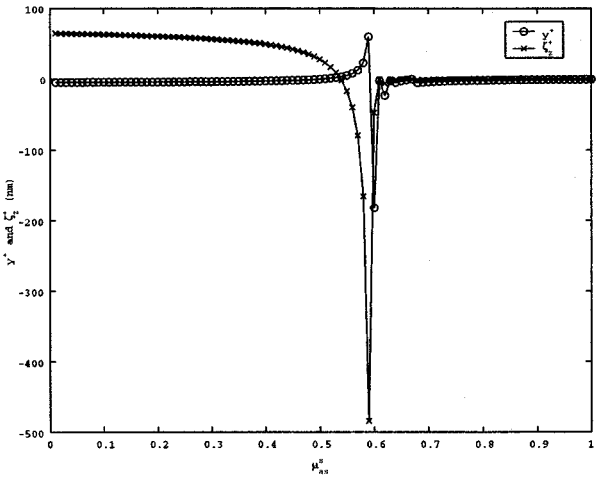

Fig. 19. The effect of changing μ_{as}^s on y^+ and ζ_z^+.

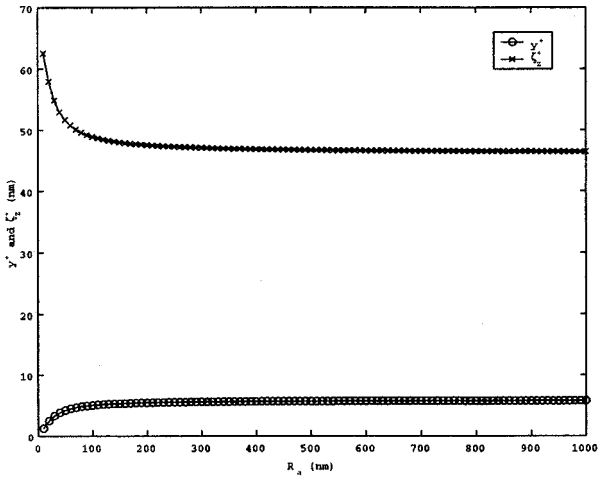

Fig. 20. The effect of changing R_a on y^+ and ζ_z^+.

pushing. Moreover, μ_{as}^s effect is tested as shown in Fig. 19. From the figure, a μ_{as}^s value around 0.6 results in a switching of y^+ and ζ_z^+ behavior. This is due to the fact that, at $\mu_{as}^s = \tan\beta$, F_z^c has a singular point, and changes its sign from "$-$" to "$+$." Finally, the change in R_a results in the effect shown in Fig. 20. For $R_a > 150$ nm, there is almost no change in y^+, while it becomes exponentially smaller for $R_a < 150$ nm (the reverse for ζ_z^+).

In the experiments, the proposed control strategies are applied for pushing 242- and 484-nm radii Au-coated latex particles. During the experiments, the cantilever parameters are $R_t = 30$ nm, $k_c = 8$ N/m, $L_x = 50$ μm, $L_y = 155$ μm, and $L_z = 6.5$ μm. The motion speed is around $V = 1$ μm/s with $\Delta = 10$ nm motion steps at 10-ms intervals. Contact force threshold $T_z = 120$ nN, $h_{\text{set}} = 1.2R_a$, $\alpha = 15°$, $f_r = 133.3$ kHz, $f = 133.4$ kHz, and $A = 100$ nm. At first, the constant height control is used for pushing $R_a = 484$ nm radius particles where the before and after top-view high-resolution ($\times 5000$) optical microscope images, and F_z^c data are given in Fig. 21. From the F_z^c data, C_1 contact and C_2 shearing points can be detected, and there is no contact loss point C_3 for this pushing. However, in some cases, C_3 is detected as in Fig. 22. Here, after C_2, the particle rotates and the tip is separated from the particle. Then, the pushing is stopped, and repeated.

For the constant contact force control, a 242-nm-radius particle is pushed with $F_z^* = 190$ nN reference value. Initial and final images of the pushing operation are shown in Fig. 23 where the particle is pushed around 0.87 μm along the y axis from the OM and AFM image display measurements. Also, from the F_z^c and z position data during the pushing operation as given in Fig. 24, the distance between C_2 and target points are measured as 0.84 μm which is very close to the real motion. Furthermore, z-positon control can track the F_z^* with a peak-to-peak tracking error of 10 nN, and the positioning accuracy is around 30 nm.

Constant height pushing can be utilized for predicting the particle motion behavior. From the experimental results, the following behavior types are observed: pure sliding [Fig. 25(a)] as a linear slope, rolling [Fig. 25(b)] as periodic curve structure, and rotation [Fig. 25(c)] as two successive peak structures. For our surface and particle material and friction design, stick–slip motion is not observed, but, it can be observed as a saw-tooth structure motion depending on the design. Thus, by the online recognition of the F_z^c

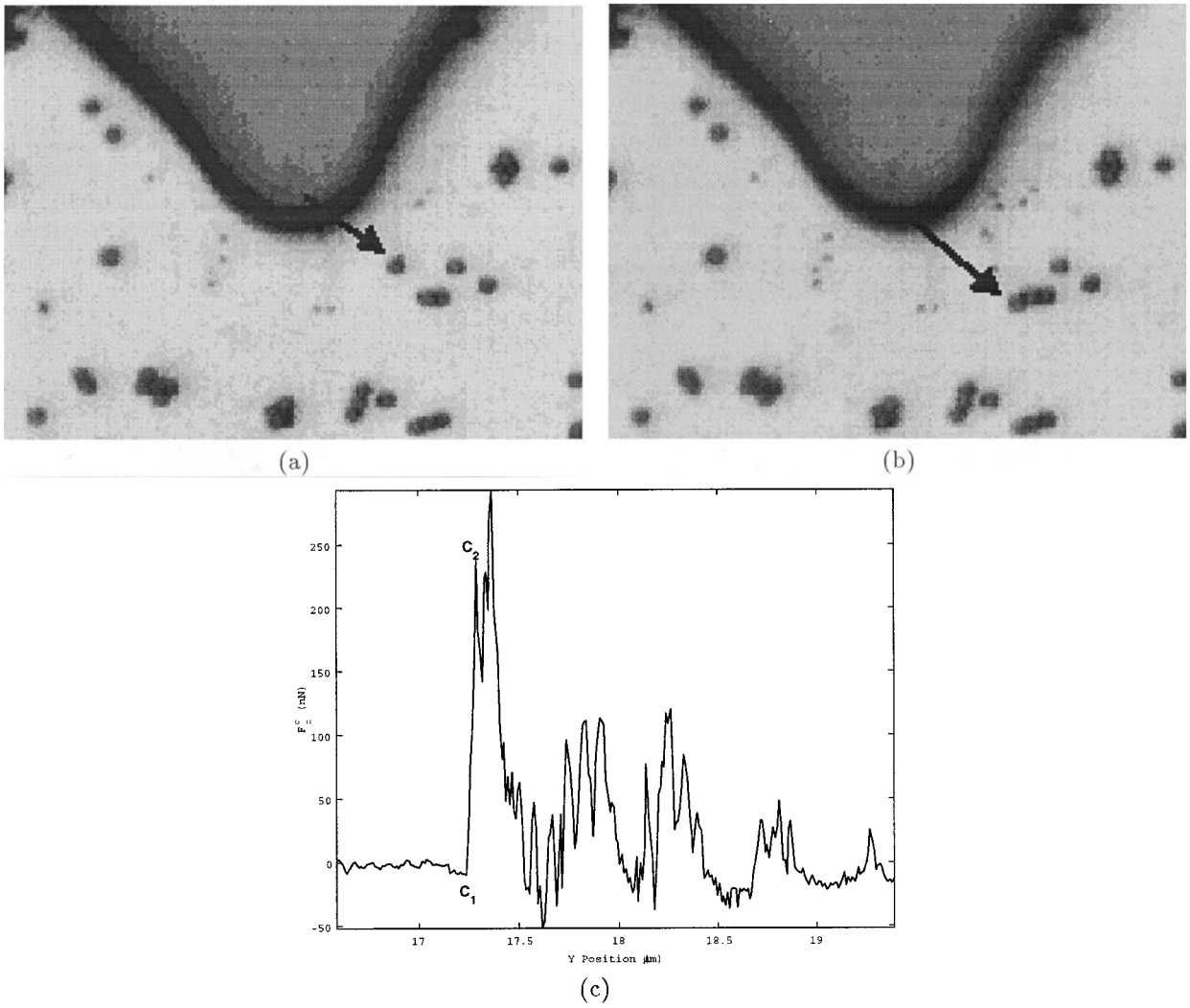

Fig. 21. Pushing a 484-nm radius latex particle using the constant height control where the high-resolution optical microscope top-view images of (a) initial and (b) final positions, and (c) F_z^c data are shown.

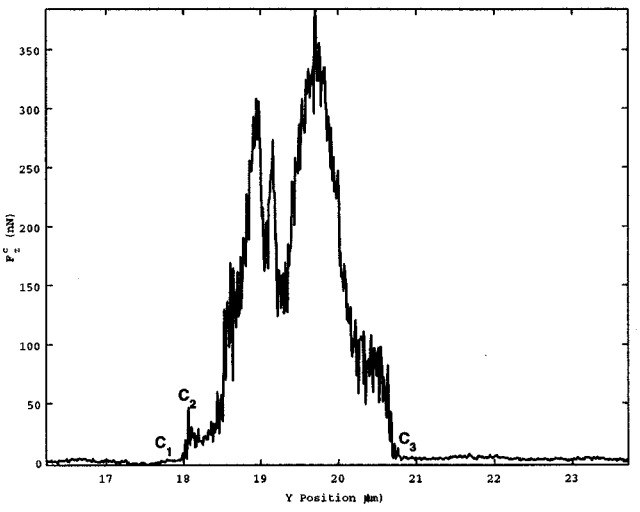

Fig. 22. Tip–particle contact loss example data during the pushing operation.

data, motion behavior can be recognized, and a real-time predictive display of the particle motion becomes possible which reduces the problem of the real-time visual feedback during the pushing operation.

IX. Conclusion and Discussions

In this paper, a nanoparticle manipulation system using an AFM as the manipulator, and force and topology sensors, has been proposed. Modeling and control of the AFM cantilever tip and particle interaction has been realized for moving particles with sizes less than 1 μm on an Si substrate in 2-D. Particle manipulation experiments are realized, and it is shown that the system can be utilized in 2-D nanoparticle assembly by an accuracy of around 20–30 nm using the proposed pushing strategies.

The problems and possible solutions of the proposed nano manipulation system are as follows.

1) Real-time visual feedback at the nano scale using scanning probe microscopes is almost not possible since scanning a surface takes a long time and, during the manipulation phase, the tip is utilized only for manipulation and

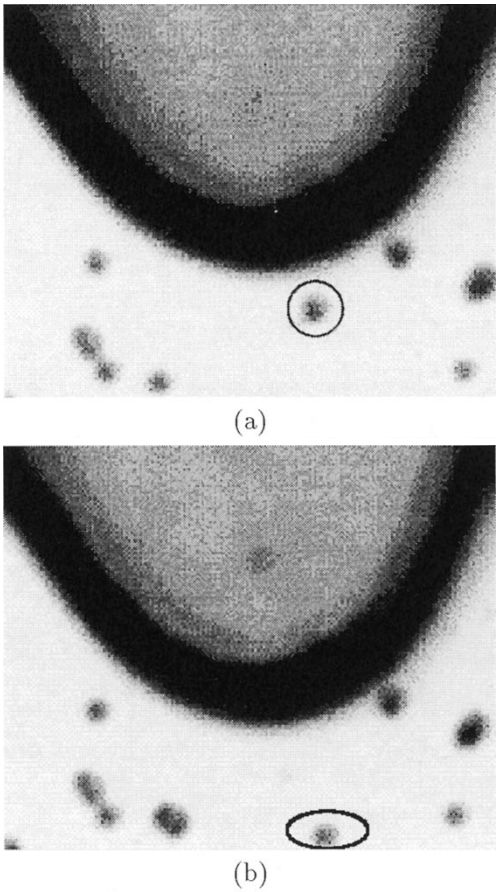

Fig. 23. Constant contact force-controlled pushing of a 242-nm radius latex particle (a) before and (b) after pushing images.

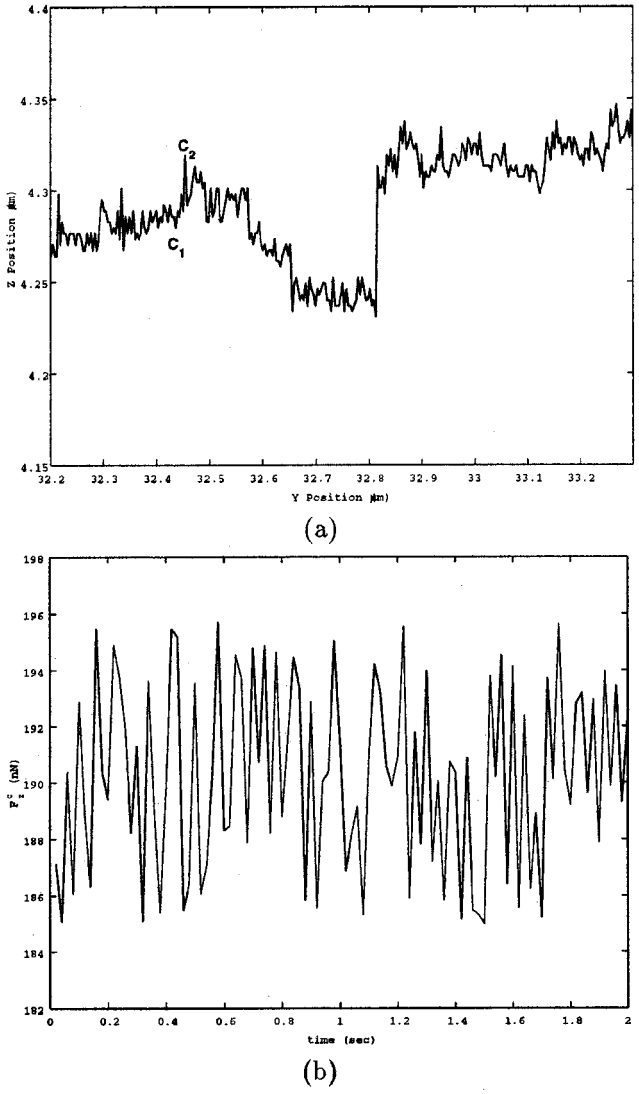

Fig. 24. Constant contact force-controlled pushing (a) z position and (b) F_z^c data.

cannot be used as the topology sensor simultaneously. Solutions to this problem are the following.

- One is by using the real-time force feedback to compensate the visual errors during the manipulation (the approach in this paper).
- Another is by using a far-field visual sensor such as an SEM. Here, there are additional problems introduced such that the SEM necessitates a vacuum environment which limits the mechanical design and increases the cost; it can be used only for (semi)conducting and some special nonconducting materials, its best resolution is around 5 nm, and it can only provide 2-D information. Furthermore, high-resolution OM can also be used depending on the application. However, it is limited as to application, and 2-D. Thus, if AFM and OM are integrated together, it could be a promising combination (also, this kind of combination is desirable for all manipulation systems since a rough micro imaging simplifies the initial setting and alignment operations such as in our system).
- By the proposed force models, the behavior of the manipulated objects and manipulators can be *animated* (augmented reality) by the real-time experimental data and physical predictive display.
- An array of multiple AFM cantilevers can enable parallel and fast scanning of the surfaces [26]. However, many cantilevers add the complexities of simultaneous actuation, control and alignment, image merging, etc., types of problems.

2) Sample preparation for the micro/nano scale object pushing applications is challenging. The frictional properties of the object and substrate interface, the adhesional forces, environmental conditions, and object fixation chemicals are all specific to the material types and object sizes. Thus, chemistry and material science are indispensable backgrounds for good sample fixation and material selection.
3) During pushing, torsional deflection measurement could be advantageous for measuring frictional forces directly. For this purpose, an optical deflection detection setup can be used, although this kind of detection limits the motion of the cantilever. The best choice could be a piezoresistive torsional deflection detection system [27].
4) Fast user-defined precision positioning with few-nanometer accuracy is necessary for reliable and *repeatable* manipulation tasks. Thus, open-loop stages are almost not

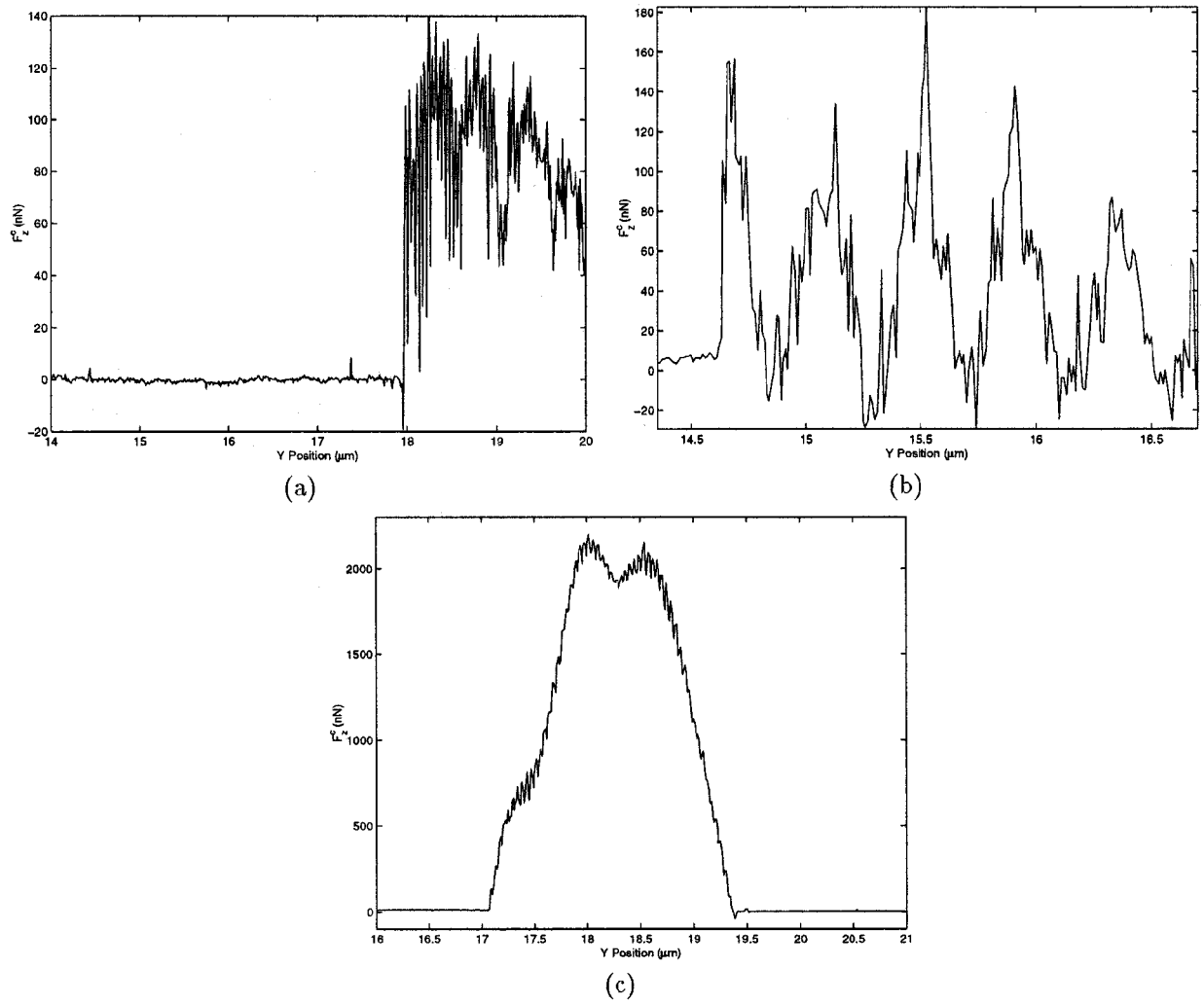

Fig. 25. Particle motion behavior types during pushing. (a) Pure sliding. (b) Rolling. (c) Rotation.

reliable, and the use of sensor-integrated stages is one possible solution. Most accurate stages utilize the capacitive sensors, although there are many problems of precision mechanics, thermal drift, electrical noise, environmental disturbances, and etc. Also, another problem is the slow bandwidth of the stage due to the increased mass, i.e., reduced resonance frequency, when the sensors are integrated.

5) Since the interactions at the micro/nano scale are mostly nonlinear and coupled, *intelligent*, stable and robust manipulation control strategies should be introduced. A task-based user interface reduced the intelligence necessity of the proposed system.
6) From the experiments, it is observed that even though the environmental parameters are controlled according to the adhesion force modeling and control, there still may be sticking problems in air conditions due to the large capillary forces, and produced electrostatic forces during contacting and manipulating objects. Therefore, manipulation in liquid could be a solution since these forces are largely reduced. However, in liquid environments, liquid flow instabilities and a double-layer type of new forces are introduced, and these forces should be controlled delicately. Furthermore, liquid manipulation is a crucial target for bioengineering where *in situ* biological object manipulation can become possible.
7) Piezoresistive cantilevers are novel tools for future micro/nano robots in the sense of integrated sensor-type manipulation tools. However, these types of sensors have the electronic and thermal noise and drift problems as compared to the optical detection cantilevers [28] and, thus, have less resolution. Thus, special care should be taken for controlling these noises with temperature control and low-noise electronics.
8) The proposed micro/nano force models all assume continuum mechanics modeling. However, going to the tens of nanometers, quantum effect and other types of discontinuous interatomic forces become more dominant. Therefore, molecular dynamics modeling or quantum electrodynamical models should be used for detailed behavior understanding, although they require intensive computation.
9) Using one AFM cantilever is limited to the simple mechanical manipulations such as pushing, cutting, drilling,

etc. More complex manipulation tasks such as pick and place are unsolved challenging problems at the nano scale.

As future work, the manipulation operations will be realized in a liquid environment for reducing the capillary and electrostatic forces, and for biological object manipulation. Also, 3-D pick-and-place manipulation is targeted using two cantilevers or adhesive chemicals.

ACKNOWLEDGMENT

The authors would like to thank Park Scientific Instruments Company for providing the piezoresistive cantilevers.

REFERENCES

[1] T. Junno, K. Deppert, L. Montelius, and L. Samuelson, "Controlled manipulation of nanoparticles with an atomic force microscopy," *Appl. Phys. Lett.*, vol. 66, pp. 3627–3629, June 1995.

[2] D. Schafer, R. Reifenberger, A. Patil, and R. Andres, "Fabrication of two-dimensional arrays of nanometric-size clusters with the atomic force microscopy," *Appl. Phys. Lett.*, vol. 66, pp. 1012–1014, Feb. 1995.

[3] R. W. Stark and S. Thalhammer *et al.*, "The afm as a tool for chromosomal dissection—The influence of physical parameters," *Appl. Phys. A*, vol. 66, pp. 579–584, Mar. 1998.

[4] M. Falvo, R. Superfine, and S. Washburn *et al.*, "The nanomanipulator: A teleoperator for manipulating materials at the nanometer scale," in *Proc. Int. Symp. Science and Technology of Atomically Engineered Materials*, Richmond, VA, Nov. 1995, pp. 579–586.

[5] M. Sitti and H. Hashimoto, "Tele-nanorobotics using atomic force microscope," in *Proc. IEEE/RSJ Int. Conf. Intelligent Robots and Systems*, Victoria, BC, Canada, Oct. 1998, pp. 1739–1746.

[6] T. Ondarcuhu and C. Joachim, "Combing a nanofiber in a nanojunction," *Nanotechnol.*, vol. 10, no. 1, pp. 39–44, 1998.

[7] T. R. Ramachandran, C. Baur, and A. Bugacov *et al.*, "Direct and controlled manipulation of nanometer-sized particles using the noncontact atomic force microscope," *Nanotechnol.*, vol. 9, no. 3, pp. 237–245, 1998.

[8] R. Resch and C. Baur *et al.*, "Manipulation of nano particles using dynamic force microscopy: Simulation and experiments," *Appl. Phys. A*, vol. 67, pp. 265–271, Sept. 1998.

[9] C. Baur and A. Bugacov *et al.*, "Nanoparticle manipulation by mechanical pushing: Underlying phenomena and real-time monitoring," *Nanotechnol.*, vol. 9, no. 4, pp. 360–364, 1998.

[10] A. Requicha, C. Baur, and A. Bugacov *et al.*, "Nanorobotic assembly of two-dimensional structures," in *Proc. IEEE Int. Conf. Robotics and Automation*, Leuven, Belgium, 1998, pp. 3368–3374.

[11] L. T. Hansen and A. Kuhle *et al.*, "A technique for positioning nanoparticles using an atomic force microscope," *Nanotechnol.*, vol. 9, no. 4, pp. 337–343, 1998.

[12] M. Sitti and H. Hashimoto, "Teleoperated nano scale object manipulation," in *Recent Advances on Mechatronics*, O. Kaynak, S. Tosunoglu, and M. J. Ang, Eds. Singapore: Springer-Verlag, 1999, pp. 322–335.

[13] M. Sitti, "Teleoperated 2-d micro/nanomanipulation using atomic force microscope," Ph.D. dissertation, Dep. Elect. Eng., Univ. Tokyo, Tokyo, Japan, Sept. 1999.

[14] T. Kasaya, H. Miyazaki, S. Saito, and T. Sato, "Micro object handling under SEM by vision-based automatic control," in *Proc. IEEE Int. Conf. Robotics and Automation*, Detroit, MI, 1999, pp. 2189–2196.

[15] M. Sitti and H. Hashimoto, "Two-dimensional fine particle positioning under optical microscope using a piezoresistive cantilever as a manipulator," *J. Micromechatron.*, to be published.

[16] F. Arai, D. Ando, and T. Fukuda, "Micro manipulation based on micro physics: Strategy based on attractive force reduction and stress measurement," in *Proc. IEEE Int. Conf. Robotics and Automation*, Pittsburgh, PA, 1995, pp. 236–241.

[17] J. Israelachvili, *Intermolecular and Surface Forces*, 2nd ed. London, U.K.: Academic, 1992.

[18] J. Crassous, E. Charlaix, H. Gayvallet, and J. Loubert, "Experimental study of a nanometric liquid bridge with a surface force apparatus," *Langmuir*, vol. 9, no. 8, pp. 1995–1998, 1993.

[19] M. Sitti, S. Horiguchi, and H. Hashimoto, "Tele-touch feedback of surfaces at the micro/nano scale: Modeling and experiments," in *Proc. IEEE/RSJ Int. Conf. Intelligent Robots and Systems*, Oct. 1999, pp. 882–888.

[20] D. Sarid, J. P. Hunt, and R. K. Workman *et al.*, "The role of adhesion in tapping-mode atomic force microscopy," *Appl. Phys. A*, vol. 66, pp. 283–286, Mar. 1998.

[21] J. Colchero, E. Meyer, and O. Marti, "Friction on atomic scale," in *Handbook of Micro/Nano Tribology*, 2nd ed. Boca Raton, FL: CRC Press, 1999, pp. 273–333.

[22] T. R. Hicks and P. D. Atherton, *The Nano Positioning Book*. Bracknell, U.K.: Queensgate Inst., 1997.

[23] U. Rabe, J. Turner, and W. Arnord, "Analysis of the high-frequency response of atomic force microscope cantilevers," *Appl. Phys. A*, vol. 66, pp. 277–282, Mar. 1998.

[24] M. Sitti and H. Hashimoto, "Tele-nanorobotics using atomic force microscope as a manipulator and sensor," *Adv. Robot. J.*, vol. 13, no. 4, pp. 417–436, 1999.

[25] M. Tortonese, R. C. Barrett, and C. F. Quate, "Atomic resolution with an atomic force microscope using piezoresistive detection," *Appl. Phys. Lett.*, vol. 62, pp. 834–836, Feb. 1993.

[26] S. Minne, S. Mannalis, and C. Quate, "Parallel atomic force microscopy using cantilevers with integrated piezoresistive sensors and integrated piezolectric actuators," *Appl. Phys. Lett.*, vol. 67, pp. 3918–3920, Dec. 1995.

[27] J. Brugger, J. Burger, M. Binggeli, R. Imura, and N. Rooij, "Lateral force measurements in a scanning force microscope with piezoresistive sensors," in *Proc. 8th Int. Conf. Solid-State Sensors and Actuators, and Eurosensors*, Stockholm, Sweden, June 25–29, 1995, pp. 636–639.

[28] O. Hansen and A. Boisen, "Noise in piezoresistive atomic force microscopy," *Nanotechnol.*, vol. 10, no. 1, pp. 51–60, 1999.

Metin Sitti (S'94–M'00) received the B.Sc. and M.Sc. degrees in electrical and electronic engineering from Bogazici University, Istanbul, Turkey, and the Ph.D. degree in electrical engineering from the University of Tokyo, Tokyo, Japan, in 1992, 1994, and 1999, respectively.

He was with the CAD/CAM Robotics Department, TUBITAK Marmara Research Center, Kocaeli, Turkey, as a Research Engineer during 1994–1996, working on visual servoing, computer vision, and robot control projects. He is currently a Post-Doctoral Research Scholar in the Department of Electrical Engineering and Computer Sciences, University of California, Berkeley. His research interests include micro/nano-mechatronics, biomimetic robotics, biomicroelectromechanical systems, telerobotics, haptic interfaces, scanning probe microscopy, and robot vision and control.

Dr. Sitti was a recipient of the Monbusho Research Scholarship during his study in Japan. He received the Nakayama Prize for the best paper presented at the IEEE/RSJ International Conference on Intelligent Robots and Systems in 1998. He is a member of the Robotics Society of Japan.

Hideki Hashimoto (S'83–M'84) received the B.Sc., M.Sc., and Dr.Eng. degrees in electrical engineering from the University of Tokyo, Tokyo, Japan, in 1981, 1984, and 1987, respectively.

He is currently an Associate Professor with the Institute of Industrial Science, University of Tokyo. From 1989 to 1990, he was a Visiting Scientist in the Laboratory for Information and Decision Systems and the Laboratory for Electromagnetics and Electronics Systems, Massachusetts Institute of Technology, Cambridge. His research interests are in the areas of robotics, control, intelligent transportation systems, and human–machine interfaces.

Prof. Hashimoto is an active member of the IEEE Industrial Electronics and IEEE Robotics and Automation Societies, having served on the Administrative Committees of both. He is also a member of the Japanese Society of Instrument and Control Engineers, Institute of Electrical Engineers of Japan, and Robotics Society of Japan.